ACS Photonics

Article

Cite This: ACS Photonics XXXX, XXX, XXX−XXX

Mislocalization in Plasmon-Enhanced Single-Molecule Fluorescence Microscopy as a Dynamical Young's Interferometer

Harrison J. Goldwyn,[†] Kevin C. Smith,[‡] Jacob A. Busche,[†] and David J. Masiello*[,†]

[†]Department of Chemistry, University of Washington, Seattle, Washington 98195, United States

[‡]Department of Physics, University of Washington, Seattle, Washington 98195, United States

Supporting Information

ABSTRACT: Mislocalization is a quantitative measure of the inability to locate the positions of individual molecular emitters in plasmon-enhanced super-resolution fluorescence microscopy. It is due to an unfortunate side-effect that scrambles the spatial profile of a molecule's fluorescence signal when plasmonic nanoantennas are introduced to boost that signal. In this article, we present an understanding of the mislocalization problem in plasmon-enhanced super-resolution fluorescence microscopy based upon a simple and intuitive theoretical model. In particular, we derive an analytic expression for mislocalization and demonstrate explicitly how it depends upon both the macroscopic interference of the coherent emission from molecular and plasmonic emitters and the microscopic dynamics of the coupled system. To derive this expression, we draw upon an analogy to the Fano interference problem and show that the spatial asymmetry in the intensity profile can be encapsulated into a single effective parameter that depends rigorously upon basic system properties. We further elucidate the causes of mislocalization within the context of hybridization between molecular and plasmonic emitters and show analytically how the localization error depends upon the relative separation, orientation, detuning, and polarizability of the emitters. Lastly, we derive a new model-based form of the plasmon-enhanced single-molecule fluorescence image for specified molecular dipole orientations and demonstrate that it significantly outperforms standard Gaussian fitting in locating the position of the molecule.

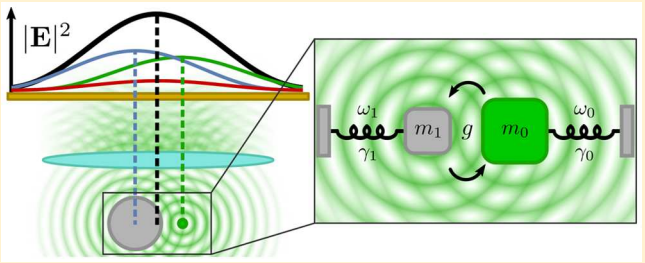

KEYWORDS: *plasmon-enhanced super-resolution fluorescence microscopy, mislocalization, plasmon hybridization, Fano interference*

Super-resolution fluorescence microscopy[1−7] has today reached spatial resolutions on the order of 20 nm[8] while providing molecular specificity in environments inaccessible to near-field probing such as live biological systems.[9−11] By switching molecules one at a time between emissive and nonemissive states,[12,13] such microscopies infer the location of each emitter from the centroid position of their isolated fluorescence signals. The intrinsically weak intensity of these images, however, limits localization precision and has motivated the incorporation of plasmonic nanoantennas known to boost the signal from individual molecules.[14−16] Unsurprisingly though, the image centroid no longer encodes the exact molecular position when both molecule and plasmonic nanoantenna are within the same diffraction-limited spot. Instead, the Airy disk pattern associated with a microscope's point spread function (PSF) reports a convolution of the emission from both sources, with its maximum lying along the line connecting the two, potentially even lying external to the sources. Naively, one might subtract the isolated nanoantenna's PSF from the observed image to reclaim the location of the molecule as the centroid of a two-dimensional Gaussian fit. However, the plasmon-enhanced image is not simply the sum of PSFs of each emitter, but instead depends upon both the (1) underlying microscopic dynamical interaction between molecular emitter and induced polarization in the nanoantenna and (2) the macroscopic radiative interference between their resulting fields. The difference between the apparent position dictated by the Gaussian maximum and the exact molecular position is commonly called the localization error or mislocalization.

Here we present an idealized yet fully analytical model of mislocalization based upon the radiative emission of two coupled and interfering dipoles, one representing the fluorescent molecule and the other representing the polarization induced in a nearby metallic nanoantenna. A vast body of literature has already been devoted to imaging molecular emitters in the vicinity of plasmonic metal surfaces and nanoparticles; see, for example, ref 17 for a recent review. Among this work, both experimental and computational efforts have been made to elucidate the physical phenomena underlying mislocalization in plasmon-enhanced single-molecule optical imaging. Specifically, the image centroid has been observed to shift toward the geometric center of the nanoantenna, even at molecule−nanoantenna separations where enhancement is not expected, a feature that has been

Received: March 22, 2018
Published: May 9, 2018

DOI: 10.1021/acsphotonics.8b00372
ACS Photonics XXXX, XXX, XXX−XXX

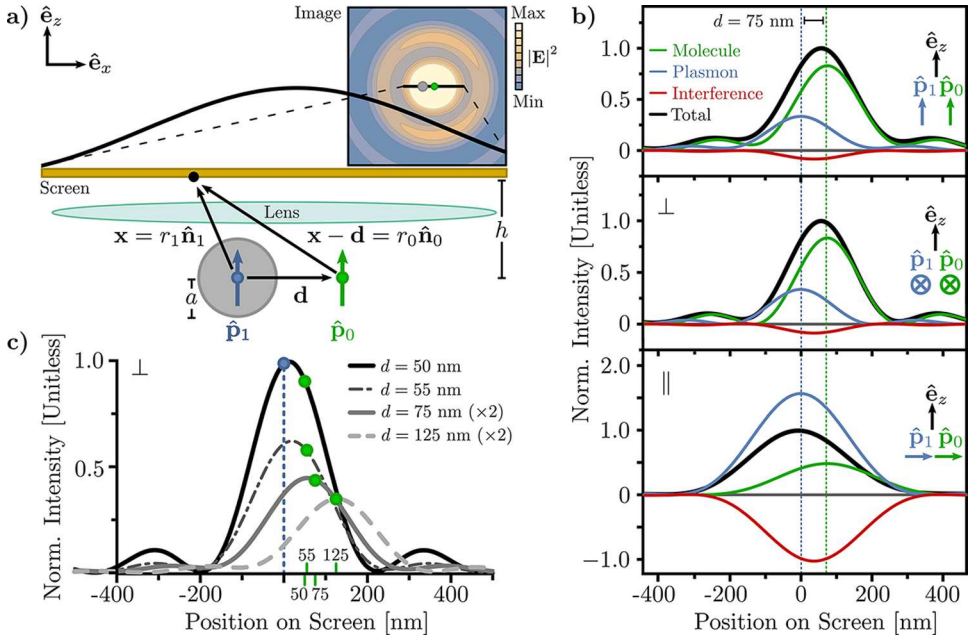

Figure 1. Plasmon-enhanced single-molecule fluorescence images. (a) Illustration of a fluorescent molecule (green dipole) and plasmonic nanoantenna (blue dipole) separated by the distance $\mathbf{d} = d\hat{\mathbf{e}}_x$. The dipole radiation fields are diffracted through a lens and imaged on the screen at (x, y, $z = h$). (b) Calculated intensity images (black) for all three unique dipole emitter orientations are displayed; from top to bottom, the orientations are named as coaxial ($\hat{\mathbf{p}} = \hat{\mathbf{e}}_z$), perpendicular ($\hat{\mathbf{p}} = \hat{\mathbf{e}}_y \perp \mathbf{d}$), and parallel ($\hat{\mathbf{p}} = \hat{\mathbf{e}}_x \parallel \mathbf{d}$). Also plotted are the molecule PSF (green), plasmon nanoantenna PSF (blue), and interference function (red) that sum to form each image. Comparison between the image and its components illustrates the complexity of the observable. (c) A progression of images versus molecule−nanoantenna separation is displayed for dipoles oriented $\perp \mathbf{d}$. The true position of the molecule has been explicitly labeled on the axis (thin tick marks) and curves (green circles) as an aid for the eye.

related to the portion of radiated power directed through the nanoantenna instead of emitted directly from the molecule to free space using numerical electrodynamics simulation.[18] By specifying the exact molecule location relative to the nanoantenna with molecular spacers, mislocalization has been quantitatively extracted from experiment,[19,20] even for three-dimensional systems with additional geometric mislocalization caused by projection onto a two-dimensional image.[21] Unintuitively, the image centroid has also been observed outside of the region between the emitters in both experiment and simulation.[22−25] Reference 23 suggested this observation to be a result of interference between the molecule and nanoantenna emission and presented an intuitive explanation based on Young's interference. References 18−25 use electromagnetic simulation to interpret observation as well as to explore dependence upon certain experimentally accessible parameters. Such simulations are useful for these purposes, but can obscure the physics in that they provide no analytic understanding of the underlying physical mechanisms. For spherical nanoantenna geometries, Mie theory provides a middle ground, combining analytical insight with simulation. Toward understanding the origins of mislocalization in surface-enhanced Raman scattering,[26] generalized Mie theory has demonstrated the importance of interference among higher-order plasmon modes on image distortion when the molecule is located within the fluorescence quenching zone ($\lesssim$5 nm from the nanoantenna surface) necessary for Raman scattering. Despite this body of work, to date, there has been no simple theoretical model that describes the mislocalization problem completely analytically. Such a model is important because it makes explicit the dependence of mislocalization upon each parameter, devoid of the complexity of Mie theory and obfuscation by electrodynamics simulation. It is the purpose of this paper to provide a model containing the minimal ingredients necessary to reproduce observation while clearly demonstrating the dependence of mislocalization on basic system parameters.

In the following, we begin by reviewing Young's double-slit experiment and make an analogy between the wave mechanics of two-slit diffraction and a pair of radiating dipole oscillators as suggested in ref 23. With the second dipole representing the nanoantenna polarization induced by the first, we then develop a description of their coupled dynamics and resulting electromagnetic radiation. After focusing this radiation with a lens, parallels are drawn between Young's diffraction pattern and the image, where the latter incorporates the mutual, self-consistent coupling between molecular dipole and plasmonic nanoantenna. In analogy to Fano's characterization of spectral antiresonance line shapes in terms of basic parameters,[27] we derive an analytical measure of the system's fluorescence mislocalization that depends only upon the distance- and orientation-dependent dipole−dipole coupling strength and nanoantenna polarizability. Lastly, we compare our analytical image intensity to that of full-wave numerical electrodynamics simulation of the coupled system and demonstrate that fitting our model to the numerically exact image of a dipole-driven gold nanoantenna significantly outperforms Gaussian fitting to the same image in the determination of molecular position. Taken together our work provides a critically needed understanding of the origins of mislocalization in plasmon-enhanced super-resolution fluorescence imaging and can be used to extract a more accurate estimate of the molecule's position than is provided by current methods.

DOI: 10.1021/acsphotonics.8b00372
ACS Photonics XXXX, XXX, XXX−XXX

ANALOGY BETWEEN TWO-SLIT INTERFERENCE AND TWO-DIPOLE EMISSION

An illustration of a coupled molecule−nanoantenna system together with a convoluted signal typical of plasmon-enhanced single-molecule fluorescence is displayed in Figure 1a. The system image behaves according to the following generic intensity

$$I(x, y) = \frac{c}{8\pi}|\mathbf{E}_0 + \mathbf{E}_1|^2 = \frac{ck^6}{8\pi}[|p_0|^2 f_{\mathrm{PSF}}(x, y; d) + |p_1|^2 f_{\mathrm{PSF}}(x, y) + 2|p_0||p_1| f_{\mathrm{IF}}(x, y; d)\cos\Phi] \quad (1)$$

measured on a photodetector positioned at height $z = h$ above and parallel to the (x, y) plane containing the sources. Independent molecule and nanoantenna PSFs (f_{PSF}) contribute to this signal, as does an interference function (f_{IF}). Each component is scaled by a separation- and orientation-dependent dipole amplitude (p_0 for the molecule and p_1 for the nanoantenna) that determines the relative weighting of their individual PSFs as well as that of the interference; the latter is further modulated by a phase Φ dictating the sign of the interference, i.e., constructive or destructive. Figure 1b and c show the effects of dipole orientation relative to separation ($\mathbf{d} = d\hat{\mathbf{e}}_x$) upon the image as well as its underlying components.

Although the intensity in eq 1 is expressed in the language of diffracted-limited imaging, it is a general description of wave interference from two distinct sources. With the functional form of f_{PSF} and f_{IF} kept general for now, qualitative intuition for the shape and apparent centroid position of a plasmon-enhanced fluorescence image can be gained by analogy to the double-slit experiment. When the slit size is small in comparison to the slit separation d and distance to the detector h, the diffracted waves emanating from the slits appear spherical as if emitted by two oscillating dipoles $\mathbf{p}_i(t) = |p_i|e^{-i(\omega t-\phi_i)}\hat{\mathbf{p}}_i$ (i = 0, 1), each located within a slit. Figure 2 displays the duality between a plane wave passing through two slits and two dipole emitters. Panel a illustrates the case of normal incidence where there is no inherent phase difference between spherical wave sources, while panel b illustrates the case of oblique incidence with phase difference $\Delta\phi = \phi_1 - \phi_0$ depending upon the incident field direction.

If the distance h between the dipole emitters and the observation screen is much larger than the emission wavelength $\lambda = 2\pi/k = 2\pi c/\omega$, then the fields from each dipole take their radiation zone forms $\mathbf{H}_i(r_i\hat{\mathbf{n}}_i) = k^2\hat{\mathbf{n}}_i \times \mathbf{p}_i(t)e^{ikr_i}/r_i$ and $\mathbf{E}_i(r_i\hat{\mathbf{n}}_i) = \mathbf{H}_i(r_i\hat{\mathbf{n}}_i) \times \hat{\mathbf{n}}_i$ in free space, where r_i connects the location of each dipole to the observation point $r_i\hat{\mathbf{n}}_i$ as displayed in Figure 1a; i.e., $r_0\hat{\mathbf{n}}_0 = \mathbf{x} - \mathbf{d}$ for the molecule and $r_1\hat{\mathbf{n}}_1 = \mathbf{x}$ for the nanoantenna. Inserting these radiated fields into eq 1 makes explicit the form of the radiative intensity I from two dipoles in free space. Visualization and discussion of this intensity is facilitated by limiting the observation to points along the x-axis of the photodetector. In the form of eq 1, the unfocused image of the intensity from two ⊥-polarized ($\hat{\mathbf{p}} = \hat{\mathbf{e}}_y \perp \mathbf{d}$) dipoles along the line $(x, 0, h)$ is

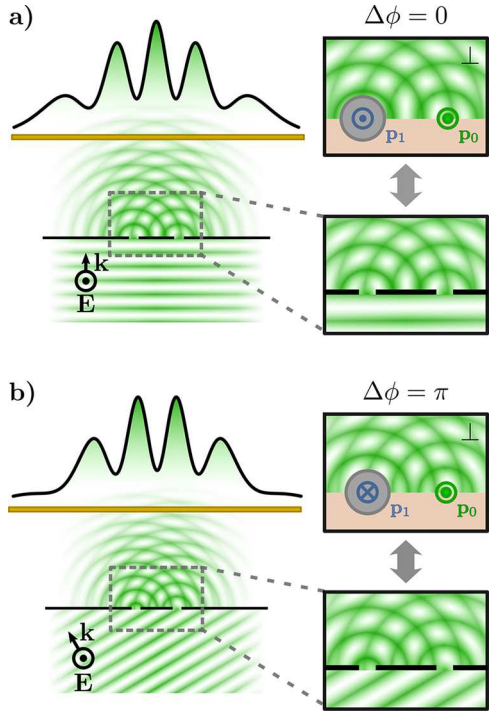

Figure 2. Analogy between Young's double slit and a pair of radiating electric dipoles. (a) A normally incident plane wave emerges from the slits as two spherical waves of equal phase, as if two dipole emitters aligned with the field polarization and oscillating in phase are located within each slit. Constructive interference appears along rays of equal path length, placing the maximum intensity between the slit/emitter positions. (b) An oblique-incident plane wave produces a relative phase that depends upon the incident angle. The case of $\Delta\phi = \pi$ is illustrated to demonstrate that destructive interference displaces the maximum intensity away from the emitters' center. Regardless of incident angle, the relative emitter brightness can shift the interference maximum asymmetrically toward and even past the brighter emitter location. Wavelength, screen height, slit/emitter separation, and interference pattern (from eq 2) are drawn to scale for dipoles of equal amplitude; however, the slit widths are not.

$$I(x) = \frac{ck^6}{8\pi}\left[|p_0|^2\frac{1}{(kr_0)^2} + |p_1|^2\frac{1}{(kr_1)^2} + 2|p_0||p_1|\frac{1}{(kr_0)(kr_1)}\cos(k(r_1 - r_0) + \Delta\phi)\right] \quad (2)$$

where $(kr_i)^{-2}$ and $[(kr_0)(kr_1)]^{-1}$ are the free space equivalents of f_{PSF} and f_{IF}. Similar forms for I can be derived for the parallel ($\hat{\mathbf{p}} = \hat{\mathbf{e}}_x \parallel \mathbf{d}$) and coaxial ($\hat{\mathbf{p}} = \hat{\mathbf{e}}_z$) dipole orientations. While the free space PSFs are different than in the focused image, they are similarly peaked above the source locations as dictated by the denominator $r_i = ((x - x_i)^2 + h^2)^{1/2}$, where $x_0 = d$ and $x_1 = 0$. The latter spatially dependent interference function is the product of two functions peaked respectively at the location of each dipole emitter. For $h \gg d$, the widths of the free space PSFs in eq 2 are large in comparison to d and combine to produce a single-peaked envelope modulated by interference fringes.

Analogy to the double-slit experiment is better demonstrated by equating the dipole amplitudes $p_0 = p_1 = p$ and approximating $r_0 \approx r_1 = r$ in the denominators of the free space PSFs. Care must be taken, however, in evaluating the spatially dependent phase $k(r_1 - r_0) = kd\sin\theta$, which can be

DOI: 10.1021/acsphotonics.8b00372
ACS Photonics XXXX, XXX, XXX−XXX

well approximated for small diffraction angles by $kd\theta$. Taken together, these approximations lead to the familiar Young's interference pattern:

$$I(\theta) \rightarrow I_{\text{inc}}[2 + 2\cos(kd\theta + \Delta\phi)] \tag{3}$$

with $I_{\text{inc}} = ck^4p^2/8\pi r^2$ inheriting the role of incident field intensity and with an additional phase factor $\Delta\phi$ dictated by the incidence angle or equivalently the relative phase between dipoles. For an aberration-free but diffraction-limited microscope, the ray interference due to the spatially dependent phase $kd\theta$ is negligible, leaving the sign of the interference dependent only on $\Delta\phi$. This absence of optical path length dependence in the phase changes the qualitative nature of the interference. Without spatial oscillations, the interference is either constructive or destructive across the entire observation window and biases the centroid toward (if constructive) or away (if destructive) from the center of the two emitters. This intuition is the beginning of understanding how observed trends in mislocalization are manifested in Young's interference.

Inserting a lens between the dipole emitters and detector changes the spatial form of the intensity quantitatively, but the PSFs remain peaked about their respective source position. The interference term is similarly peaked but at the midpoint between the emitters resulting from the cross product of the focused fields from each dipole. This means that the intuition gained from understanding the image as composed of three distinct peaked functions in double-slit interference may be applied directly to the diffraction-limited image of a microscope by replacing the fields in eq 1 with the focused and diffracted dipole fields. Analytic forms for f_{PSF} and f_{IF} for all three unique dipole orientations can be approximated by assuming the microscope to be an ideal, infinity-corrected and aberration-free optical system with numerical aperture NA = 1. Details of computing the image fields via the Debye–Wolf diffraction integral are presented in the Methods section.

COUPLED DIPOLE INTERACTION MODEL

Up to this point, the underlying microscopic dynamics of the dipole emitters and associated relative phase have been left unspecified. We now show how to model the interacting molecule–nanoantenna system as a pair of coupled dipole oscillators. In previous work,[28,29] we demonstrated the mapping of multipolar localized surface plasmon resonances onto corresponding mechanical oscillators, each with an associated effective mass m_l and resonance frequency ω_l in the quasistatic limit. $l = 1$ corresponds to the dipole plasmon mode. However, for any l, the mass is inversely proportional to the static (zero-frequency) polarizability α_{sp} and resonance frequency, the latter determined by material- and geometry-specific parameters related to both the bound and free conduction electronic response of the plasmon nanoantenna, as will be discussed later. Similar correspondence between a molecular transition (i.e., fluorescence emission) dipole moment and a harmonic oscillator follows directly from Schödinger's equation, with the transition's effective mass m_0, transition frequency ω_0, and damping constant γ_0 parametrized by the free molecule's fluorescence spectrum.

The interaction between molecular dipole and plasmonic nanoantenna is well-known to involve higher-order plasmon modes beyond the dipole whenever the two are in close proximity (shown in ref 30 to be $d - a \lesssim 10$ nm for a spherical gold nanoantenna of radius $a = 40$ nm). At such close distances, inefficient coupling of the higher-order plasmon modes to the radiation field quench the molecule's fluorescence and allow weaker molecular optical processes to persist, such as Raman scattering.[31−34] However, since this paper focuses only on understanding mislocalization in the regime where fluorescence emission is dominant ($d - a \gtrsim 10$ nm) using the most simple analytic model possible, we neglect all higher-order plasmon multipole moments and couple the remaining nanoantenna dipole mode to the molecular transition via the fully retarded dipole–dipole interaction. The resulting equations of motion describing the plasmon-enhanced single-molecule fluorescence are classical in appearance,

$$\begin{aligned}\ddot{p}_0 &= -\omega_0^2 p_0 - \gamma_0\dot{p}_0 + \tfrac{e^2}{m_0}\hat{\mathbf{p}}_0\cdot\mathbf{E}_1(\mathbf{d}) + \tfrac{2e^2}{3m_0c^3}\dddot{p}_0 + \tfrac{e^2}{m_0}E_F e^{-i\omega t}\\ \ddot{p}_1 &= -\omega_1^2 p_1 - \gamma_1\dot{p}_1 + \tfrac{e^2}{m_1}\hat{\mathbf{p}}_1\cdot\mathbf{E}_0(\mathbf{0}) + \tfrac{2e^2}{3m_1c^3}\dddot{p}_1\end{aligned} \tag{4}$$

where the physical oscillation amplitude and phase of each dipole moment are determined by the complex magnitude $|p_i|$ and phase angle $\phi_i = \tan^{-1}\text{Im}\,p_i/\text{Re}\,p_i$. Here, $(e^2/m_0)\hat{\mathbf{p}}_0\cdot\mathbf{E}_1(\mathbf{d}) \equiv (g/m_0)p_1$ and $(e^2/m_1)\hat{\mathbf{p}}_1\cdot\mathbf{E}_0(\mathbf{0}) \equiv (g/m_1)p_0$, where $g \equiv g(\mathbf{d}) \equiv e^2\hat{\mathbf{p}}_0\cdot\mathbf{G}(\mathbf{d})\cdot\hat{\mathbf{p}}_1$ is the dipole–dipole coupling strength between molecular transition dipole $\mathbf{p}_0$ and the induced polarization in the nanoantenna, the latter treated as a point dipole $\mathbf{p}_1$ located at the center of a sphere of radius a. $\mathbf{G}(\mathbf{d}) = [(3\hat{\mathbf{d}}\hat{\mathbf{d}} - 1)(1/d^3 - ik/d^2) - (\hat{\mathbf{d}}\hat{\mathbf{d}} - 1)k^2/d]e^{ikd}$ is the dyadic Green's function,[35] γ_1 is the nanoantenna's nonradiative line width, and the dipole jerk terms account for the effects of radiation reaction. $\mathbf{E}_1(\mathbf{d})$ and $\mathbf{E}_0(\mathbf{0})$ are the electric dipole fields of the nanoantenna at $\mathbf{x} = \mathbf{0}$ and molecule at $\mathbf{x} = \mathbf{d}$, each evaluated at the position of the other. Note that g is identical for the coaxial and perpendicular dipole orientations illustrated in Figure 1, and the orientation of the induced dipole $\mathbf{p}_1$ is completely determined by the molecular transition dipole $\mathbf{p}_0$ and $\mathbf{d}$ since $\mathbf{p}_1 = \alpha_1\mathbf{E}_0(\mathbf{0}) = \alpha_1\mathbf{G}(\mathbf{d})\cdot\mathbf{p}_0$. The form of $\mathbf{G}(\mathbf{d})$ also reveals that the induced plasmon dipole $\mathbf{p}_1$ in the nanoantenna will be parallel to the molecule dipole moment $\mathbf{p}_0$ only when $\mathbf{p}_0 \parallel \mathbf{d}$ or $\mathbf{p}_0 \perp \mathbf{d}$.

A fictitious harmonic electric field E_F of frequency ω is applied to the molecular oscillator to model the population of the emissive state by absorption of the real excitation field and subsequent vibrational relaxation characteristic of fluorescence. In this way the molecule oscillator represents the emissive transition dipole, and ω can therefore be interpreted as a single Fourier component of molecular fluorescence, taken here to be at the peak of the emission spectrum, i.e., at $\omega = \omega_0$. At this Stokes-shifted frequency the plasmon oscillator is not directly driven by E_F because plasmon photoluminescence is negligible in comparison to the molecule's fluorescence.[36]

Although the intense near field of the plasmonic nanoantenna will enhance molecular absorption, mislocalization is independent of the absorption rate[37] modeled here by E_F. This absorption independence of the coupled system's radiative emission profile takes its origin as a linear dependence between p_1 and p_0 in the steady-state solution to eq 4, i.e., $\mathbf{p}_1 = \alpha_1\mathbf{E}_0(\mathbf{0}) = \alpha_1\mathbf{G}(-\mathbf{d})\cdot\mathbf{p}_0$. Using this result, the focused diffraction-limited intensity at height $z = h$ presented in eq 1 can be normalized by the molecule emission $I_0 \equiv (ck^6/8\pi)|p_0|^2$ without loss of spatial information contributing to mislocalization. The image shape is then defined by

$$\frac{I(x,y)}{I_0} = f_{\text{PSF}}(x,y;d) + \left|\frac{p_1}{p_0}\right|^2 f_{\text{PSF}}(x,y) + 2\text{Re}\left[\frac{p_1}{p_0}\right] f_{\text{IF}}(x,y;d) \tag{5}$$

DOI: 10.1021/acsphotonics.8b00372
ACS Photonics XXXX, XXX, XXX−XXX

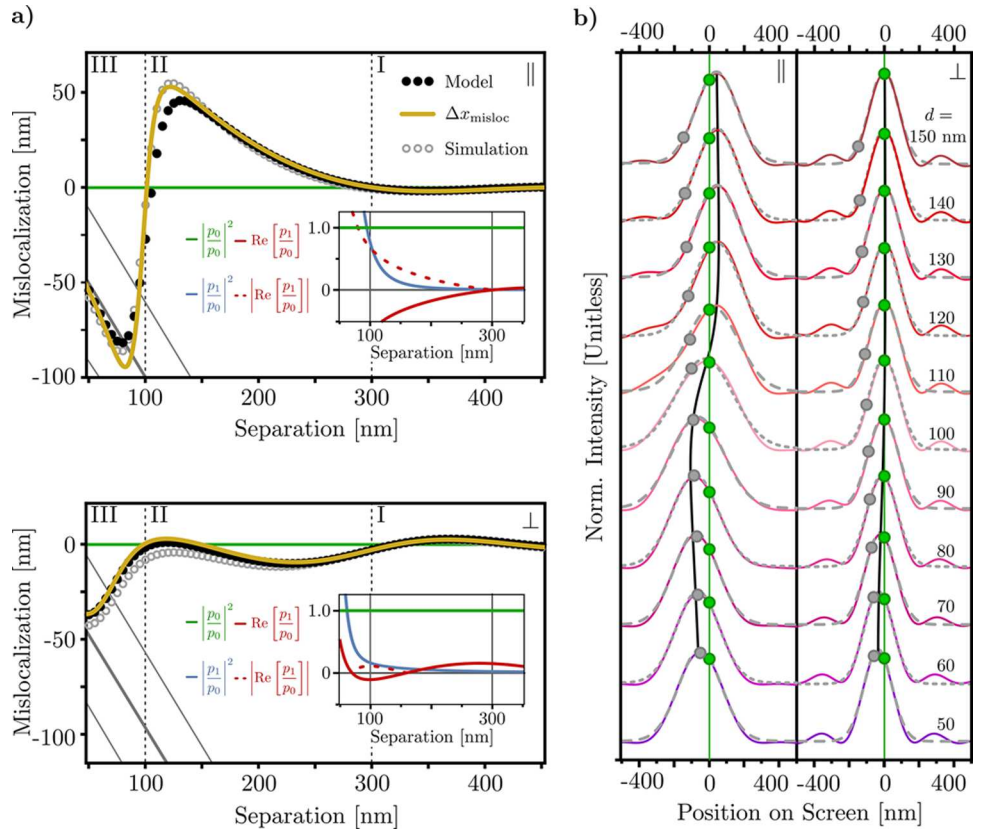

Figure 3. Gaussian mislocalization in modeled and simulated plasmon-enhanced single-molecule fluorescence images as a function of molecule−nanoantenna separation d. (a) Mislocalization for $\hat{\mathbf{p}} \parallel \mathbf{d}$ (top) and $\hat{\mathbf{p}} \perp \mathbf{d}$ (bottom) determined by fitting a two-dimensional Gaussian to electrodynamics simulation (gray circles) or to the image intensity given in eq 5 (black circles) is compared to prediction using the analytic mislocalization measure $\Delta x_{misloc}(d)$ in eq 10 (yellow). An a = 40 nm spherical gold nanoantenna in a vacuum is used in each case. The location of the molecule (green) and the locations of the center and edges (gray) of the nanoantenna are plotted for reference. Three qualitatively distinct separation regimes are marked by Roman numerals for both the ∥ and ⊥ orientations: (I) Mislocalization is negligible for $d \gtrsim 300$ nm due to fulfillment of both the Rayleigh criterion and weak coupling as $|p_1/p_0| \lesssim 0.1$. (II) As the molecule approaches the nanoparticle, the interference term scales linearly with coupling and produces significant mislocalization, while $|p_1/p_0| < 1$. (III) For $d \lesssim 100$ nm, the image centroid collapses onto the nanoantenna due to the quadratic scaling with coupling of the nanoantenna PSF amplitude. In this regime, $|p_1/p_0| \gtrsim 1$ and, therefore, the magnitude of the nanoantenna PSF surpasses both molecule PSF and interference. (b) Normalized plasmon-enhanced single-molecule images (red-purple) calculated from eq 5 are overlaid with two-dimensional Gaussian fits (gray, dashed) for both ∥ (left) and ⊥ (right) dipole orientations at separations d = 50−150 nm. Δx_{misloc} is plotted in black along with the true locations of the nanoantenna (gray circles) and molecule (green circles) as a guide for the eye. Note that the Gaussian fits are nearly indistinguishable from the main peak of the Airy disk for most separations, even when $\Delta x_{misloc} \gtrsim 10$ nm.

Note that $E_F = |\mathbf{E}_F|$ only appears within I_0 because $\mathbf{p}_0 = \alpha_0[\mathbf{E}_F + \mathbf{E}_1(\mathbf{d})] = [\alpha_0^{-1} - \mathbf{G}(\mathbf{d})\ \alpha_1\mathbf{G}(\mathbf{0})]^{-1}\mathbf{E}_F$, which clearly demonstrates that the absorption rate only scales the intensity profile and does not contribute to mislocalization. What is critical in controlling the shape of the system image is the relative amplitude of the two emitters, $p_1/p_0 = |p_1/p_0|e^{i\Delta\phi}$.

The ratio of dipole amplitudes p_1/p_0 can be determined by the equations of motion in eq 4, which approximate the electronic response of the plasmon nanoantenna as a free-electron gas. But better quantitative agreement with simulation is achieved by generalizing the nanoantenna polarizability to account for the response of the metal's bound and free electrons as

$$\frac{p_1}{p_0} = a^3\frac{\varepsilon(\omega_0) - 1}{\varepsilon(\omega_0) + 2}\frac{g(\mathbf{d})}{e^2} = \left[a^3\frac{\varepsilon_\infty - 1}{\varepsilon_\infty + 2} + \frac{e^2/m_1}{\omega_1^2 - \omega_0^2 - i\omega_0\gamma_1^R}\right]\frac{g(\mathbf{d})}{e^2} \quad (6)$$

where $\varepsilon(\omega) = \varepsilon_\infty - \omega_p^2/\omega(\omega + i\gamma_D)$ is the bulk Drude dielectric function expressed in terms of the standard Drude parameters. The first term in square brackets, $\alpha_\infty = a^3(\varepsilon_\infty - 1)/(\varepsilon_\infty + 2)$, represents the instantaneous response of the nanoantenna's bound core electrons to the molecular dipole field, while the second term, $\alpha_f(\omega_0) = \alpha_{sp}\omega_1^2/(\omega_1^2 - \omega_0^2 - i\omega_0\gamma_1^R)$, with $\alpha_{sp} = 3a^3/(\varepsilon_\infty + 2) = e^2/m_1\omega_1^2$, represents the causal response of its free conduction electrons. It is the dynamic polarizability in the second term that is important and that is described completely by the coupled equations of motion (eq 4). Writing the ratio $p_1/p_0 = \alpha_1(\omega_0)(g/e^2)$, where $\alpha_1(\omega) = \alpha_\infty + \alpha_f(\omega)$ is the polarizability of the plasmon nanoantenna, emphasizes the generality of this model since the nanoantenna may be of arbitrary shape or size as long as its polarizability can be determined.

The relative contributions to the imaged intensity in eq 5 from molecule, nanoantenna, and interference are compared as functions of separation in the insets in Figure 3a. The three terms composing eq 5 are each plotted as a function of position in the image plane in the Supporting Information to gain

DOI: 10.1021/acsphotonics.8b00372
ACS Photonics XXXX, XXX, XXX−XXX

intuition on the image composition. In these plots and in what follows, the parameters describing the isolated plasmon oscillator are determined by fitting the scattering cross section derived from the equation of motion for the uncoupled plasmon $\ddot{p}_1 + \gamma_1^R \dot{p}_1 + \omega_1^2 p_1 = (e^2/m_1)\, E e^{-i\omega t}$ to the simulated scattering cross section of an $a = 40$ nm gold sphere in vacuum, but could also be obtained from experiment. Radiation reaction effects increase the line width according to $\gamma_i^R = \gamma_i + (2e^2/3m_i c^3)\omega^2$. The resonance energy, line width, and effective mass of the nanoantenna plasmon are $\hbar\omega_1 = 2.55$ eV, $\hbar\gamma_1 \equiv \hbar\gamma_D = 0.06$ eV, and $m_1 = 8.31 \times 10^{-7} m_e$. The fluorophore parameters are obtained from the same procedure, but using the equation of motion for the uncoupled molecule emission $\ddot{p}_0 + \gamma_0^R \dot{p}_0 + \omega_0^2 p_0 = (e^2/m_0)\, E e^{-i\omega t}$ to fit typical fluorescence cross sections for dyes commonly used in super-resolution imaging. The resonance energy, line width, and effective mass of the molecule's transition dipole are $\hbar\omega_0 = 2.60$ eV, $\hbar\gamma_0 = 0.075$ eV, and $m_0 = 1.22 \times 10^3 m_e$. All other parameters, such as the coupling strength and radiation reaction force are computed from these parameters (and fundamental constants such as the mass m_e and charge $-e$ of the electron). Note that the effective mass of the plasmon is 10 orders of magnitude smaller than that of the molecular transition dipole, a fact that will be of importance in the following. This scale difference is due to the difference in polarizabilities between the two emitters, since effective mass is inversely proportional to polarizability as described above. Also note that the above parameters make the nanoantenna-molecule detuning $\omega_1^2 - \omega_0^2$ negative. However, a positive detuning would only interchange the role of constructive and destructive interference.

To aid in the analysis and interpretation of the PSF image and resulting mislocalization, it is instructive to revisit eqs 5 and 6 from the viewpoint of hybridized modes. The response of the nanoantenna core electrons and friction are temporarily neglected and the dipole−dipole coupling is restricted to the near-field interaction. These approximations, while not quantitatively exact, retain the essential features of the system while providing intuition about mislocalization based upon hybridization. As a function of dipole−dipole separation, orientation, detuning, and relative polarizability, the molecule and nanoantenna dipoles will mix to varying extent as described by the mixing angle $\beta = (1/2)\tan^{-1} 2g(\mathbf{d})/\sqrt{m_0 m_1}(\omega_1^2 - \omega_0^2)$ to produce the hybridized modes

$$p_+ = p_0\left(\frac{m_0}{m_1}\right)^{1/4}\cos\beta + p_1\left(\frac{m_1}{m_0}\right)^{1/4}\sin\beta$$
$$p_- = p_1\left(\frac{m_1}{m_0}\right)^{1/4}\cos\beta - p_0\left(\frac{m_0}{m_1}\right)^{1/4}\sin\beta \quad (7)$$

with radiative spatial profiles that reflect the degree of mixing in their asymmetry. β takes values between 0 and $\pm\pi/4$, with $\beta = 0$ corresponding to no mixing and $|\beta| = \pi/4$ corresponding to maximal mixing of the uncoupled molecule and nanoantenna modes. In terms of β, eq 5 becomes

$$\frac{I(x,y)}{I_0(\beta)} \approx \sqrt{\frac{m_1}{m_0}}\cos^2\beta\, f_{\mathrm{PSF}}(x,y;d) + \sqrt{\frac{m_0}{m_1}}\sin^2\beta\, f_{\mathrm{PSF}}(x,y) + 2\sin\beta\cos\beta\, f_{\mathrm{IF}}(x,y;d) \quad (8)$$

where $I_0(\beta) = (ck^6/8\pi\cos^2\beta)|p_0|^2\sqrt{m_0/m_1}$ and where the relative brightness $p_1/p_0 = (1/2)\sqrt{m_0/m_1}\tan 2\beta$ can be interpreted as a measure of mixing p_0 and p_1 into the hybridized molecular excitonic-plasmonic normal modes p_+ and p_-. As discussed previously, the degree of mislocalization is determined entirely by the relative weights of the three prefactors of the individual PSFs and interference function. At the separations distances of interest (i.e., $d - a \approx 10-450$ nm), $2g(\mathbf{d})/\sqrt{m_0 m_1}(\omega_1^2 - \omega_0^2) \ll 1$ and $\beta \ll 1$, justifying the small angle approximation, i.e., $p_1/p_0 \approx \sqrt{m_0/m_1}\tan\beta$. For oscillators of equal mass, this would indicate weak hybridization and produce an image dominated by the molecule PSF. However, here, the extreme mismatch in oscillator masses (or, equivalently, polarizabilities) causes the amplitude of the nanoantenna PSF to be appreciable and even dominant over the molecule PSF for relatively small values of the mixing angle, reflecting the non-negligible contribution of the plasmon nanoantenna to the normal modes of the composite system.

Fitting a two-dimensional Gaussian function to the plasmon-enhanced fluorescence image in eq 5 quantifies the balance of the molecule, nanoantenna, and interference PSFs. The resulting Gaussian centroid location relative to the exact location of the molecule—called the centroid offset or mislocalization—is plotted in Figure 3 for dipoles oriented parallel and perpendicular to $\mathbf{d}$; the third orientation with dipoles aligned along the optical axis, displayed in Figure 1a, is not shown because it is nearly identical to that of the perpendicular orientation as described above. Three qualitatively different regimes (denoted by I, II, III) are identified in Figure 3: At separations d greater than the diffraction limit, i.e., $d \gtrsim \lambda/2\mathrm{NA} \approx 240$ nm, two uncorrelated emitters would be resolvable by the Rayleigh criterion. But in this system, mislocalization remains beyond 240 nm because of the coupling-induced interference between coherent molecule and nanoantenna emission. I) This means that mislocalization is negligible only at separations $d \gtrsim 300$ nm, where both the Rayleigh criterion holds and the contribution from interference is bounded by $|p_1/p_0| \lesssim 0.1$. At these large separations, the coupling strength $|g/e^2| \lesssim 0.1/|\alpha_1(\omega_0)|$ and the mixing angle $\beta \approx 0$ as the plasmon receives minimal energy from the molecule's emissive transition. In this regime the normal modes are very weakly mixed and the molecule PSF dominates the image as in normal super-resolution microscopy. II) As the molecule approaches the nanoantenna, g and β increase and the relative amplitude $|p_1/p_0| \sim 1$. While $|p_1/p_0| < 1$, the interference begins to impact the image before the nanoantenna PSF because of its linear scaling with $\mathrm{Re}[p_1/p_0] = |p_1/p_0|\cos\Delta\phi$. If the interference is destructive, f_{IF} will subtract from the imaged intensity between the emitters and shift the centroid to the right (see Figure 1a for an illustration). If the interference is constructive, the system image is weighted toward the center of the emitters even before the nanoantenna PSF contributes. III) For $d \lesssim 100$ nm, g and β increase further and $|p_1/p_0| \gtrsim 1$. In this regime, the quadratic scaling of the nanoantenna PSF's amplitude causes the nanoantenna to dominate the image, shifting the total image onto the nanoantenna emission center or even past it slightly if the interference remains destructive.

The preceding analysis of mislocalization versus separation explains the dominant experimental observation: the centroid is much more likely to collapse onto the nanoantenna than to shift away due to destructive interference. It is only in the

DOI: 10.1021/acsphotonics.8b00372
ACS Photonics XXXX, XXX, XXX−XXX

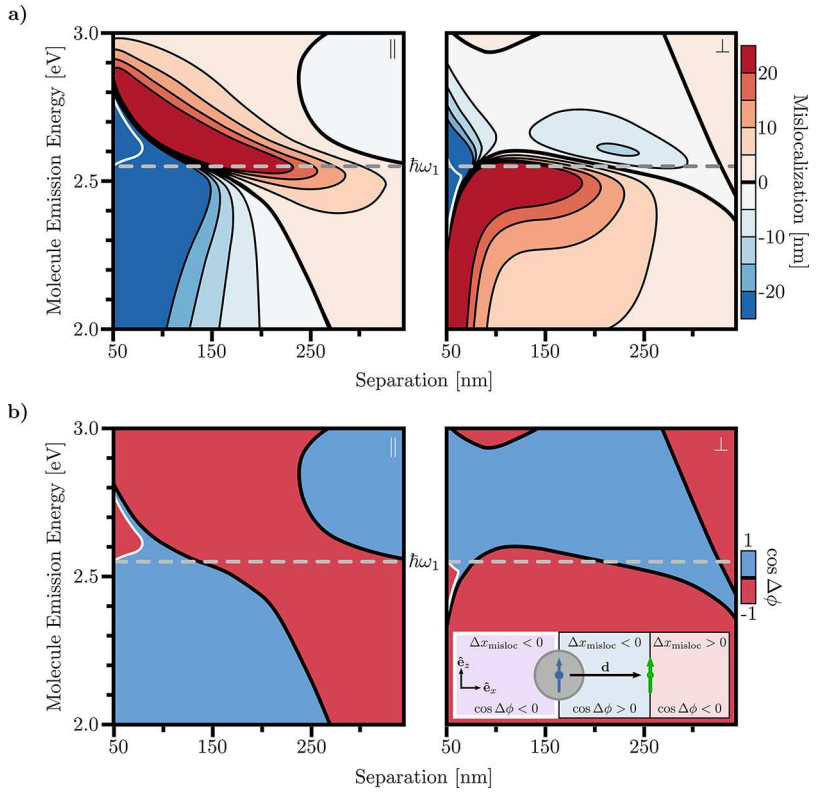

Figure 4. Correlation between mislocalization and interference quality. (a) Contour maps of mislocalization as a function of molecule emission energy $\hbar\omega_0$ and emitter separation d for ∥ (left) and ⊥ (right) dipole orientations. The fixed plasmonic nanoantenna resonance energy $\hbar\omega_1$ is marked by the horizontal line. Based on the system illustration in Figure 1a, positive mislocalization corresponds to centroid displacement to the right of the antenna and negative mislocalization corresponds to the image centroid appearing between the two emitter locations except for when $\Delta x_{misloc} < -d$ (white outline) where the centroid lies to the left of the nanoantenna. (b) Binary interference quality maps show the sign of $\cos\Delta\phi = \mathrm{Re}[p_1/p_0]/|p_1/p_0|$ as a function of $\hbar\omega_0$ and d. The inset displays the correspondence between mislocalization, interference quality, and centroid location. With constructive interference ($\cos\Delta\phi > 0$), the centroid appears in the region between the molecule and the nanoantenna. With destructive interference ($\cos\Delta\phi < 0$) the centroid may appear in either the region to the right of the molecule location or in the region to the left of the nanoantenna location, depending on the strength of the emitter−plasmon interaction. The latter case is outlined in white in (a) and (b) as well as in the inset.

intermediate separation region (II) where interference can shift the image centroid outside the two emitters. This occurrence is made more rare by the fact that interference will only be destructive for certain dipole orientations, given the nature of g to change sign as a function of $\hat{\mathbf{p}}\cdot\mathbf{d}$. Because the molecular dipole is randomly oriented in most experiments, destructive interference will often be washed out by molecules located at the same location but of different orientation. In simulation, the dipole orientation can be set explicitly and observation of positive mislocalization is more accessible. Because the plasmon PSF is always positive, the image centroid inevitably collapses onto the nanoantenna at close proximities regardless of dipole orientation. As discussed previously, this collapse of the system image centroid onto the plasmonic nanoantenna is well documented in the plasmon-enhanced single-molecule fluorescence literature. See, for example, ref 17 for a recent review.

FANO-LIKE ASYMMETRY AS A MEASURE OF MISLOCALIZATION

While the centroid offset can be predicted for arbitrary molecule-nanoantenna separation via a Gaussian fit of the intensity in eq 5, it is also possible to derive an analytic expression for the centroid offset directly from the imaged intensity function. In 1961, Fano described asymmetric antiresonance lineshapes in Helium autoionization spectra in terms of the interference between bright and dark scattering channels, and encapsulated the deviation from a symmetric line shape into an effective parameter that depends upon basic system properties.[27] The problem considered here of two coupled oscillators, one driven (i.e., the molecule, in analogy to the bright mode) and one undriven (i.e., the plasmon nanoantenna, in analogy to the dark mode), is of similar form. Interestingly, not only can such interferences arise in spectra[38] but so too can they manifest in the spatial profiles of absorbed[39] and emitted radiation. We make this analogy by factoring eq 5 into even and odd contributions about the location of the molecule projected onto the image screen, thus separating the terms that do not contribute to the centroid offset from those that do. Factoring out the spatially symmetric terms renders the image as a product of a symmetric function and a factor that is inherently antisymmetric. Taylor expansion allows us to map this factored form onto the product of a Gaussian (centered at the molecule location projected onto the image screen) with amplitude A and variance σ^2, and a line with slope η, all rigorously defined in terms of the nanoantenna polarizability α_1 and coupling strength g. All together, the spatial asymmetry of the image is characterized by the approximate image function

DOI: 10.1021/acsphotonics.8b00372
ACS Photonics XXXX, XXX, XXX−XXX

$$\frac{I(x)}{Ae^{-x^2/2\sigma^2}} \approx 1 + \eta \cdot kx \tag{9}$$

with its maximum defining the apparent molecule location, or mislocalization,

$$\Delta x_{\text{misloc}}(d) = \frac{\sqrt{1 + (2\eta k\sigma)^2} - 1}{2\eta k} \tag{10}$$

This mislocalization function is plotted versus molecule-nanoantenna separation d in Figure 3 alongside the mislocalization resulting from numerical Gaussian fits to images computed from the oscillator model as well as from full-wave numerical electrodynamics simulation of the coupled-dipole system. It is evident that $\Delta x_{\text{misloc}}(d)$ not only recovers both Gaussian-fit-based measures of mislocalization, but more importantly, makes explicit the parameters that mislocalization depends upon. Further, $\Delta x_{\text{misloc}}(d)$ enables prediction of mislocalization without need for simulation once the independent oscillators are parametrized. Although simple to implement, the explicit dependence of η and σ on d is complicated and reserved for the Supporting Information. Details of the procedure for obtaining eq 10 are presented in the Methods section.

Up to this point, the nanoantenna−molecule detuning has been fixed so that the parallel dipole orientation produces primarily destructive interference at close proximity while the perpendicular orientation is constructive. The interference quality of these two orientations has resulted in different mislocalization trends as the molecule approaches the antenna, but the relationship between mislocalization sign and interference quality ($\cos \Delta\phi$) is ubiquitous across detuning. Figure 4 expands upon this concept for a range of molecular emission energies (corresponding to the observation energy) relative to the fixed plasmon resonance energy, $\hbar\omega_1 = 2.55$ eV. For all separations, detunings, and orientations investigated, the image centroid appears between emitters when interference is constructive and outside emitters when destructive. At separations $d > 300$ nm, coupling is weak and mislocalization is minimal in all cases. Regions of large mislocalization appearing as dark red and blue in Figure 4a dominate at close molecule−nanoantenna proximity, but persist to larger separations when $\hbar\omega_1 \approx \hbar\omega_0$ because $\alpha_1(\omega_0) \propto (\omega_1^2 - \omega_0^2)^{-1}$. Near-zero detuning, the largest mislocalization at midrange $150 < d < 250$ nm lies in the regions of destructive interference for both orientations, indicating a stronger impact on the observable than constructive interference at equal coupling strength. The tendency for interference quality and mislocalization direction to be opposite for dipoles $\parallel$ and $\perp$ $\mathbf{d}$ can be qualitatively understood by considering the lowest energy arrangement of dipoles interacting through the near field only ($g_{\text{NF}} \propto d^{-3}$), i.e., head-to-tail. With fixed orientation, head-to-tail dipoles will be in-phase if $\hat{\mathbf{p}} \parallel \mathbf{d}$ but out-of-phase for $\hat{\mathbf{p}} \perp \mathbf{d}$. Quantitatively, this result appears in the opposite sign of g for these orientations, which determines the relative phase of oscillation through $\text{Re}[p_1/p_0]$. The transition between dark red and dark blue regions indicates a sharp change of the image centroid from one side of the molecule to the other as it approaches the nanoantenna. This type of transition can be seen in Figure 3a for the $\parallel$ orientation at $d = 100$ nm and is due to a flip in interference quality while the coupling is relatively strong, as illustrated in Figure 4b.

ALTERNATIVE TO GAUSSIAN FITTING

From Figure 3, it is clear that Gaussian fitting performs poorly when both emitters are located within the same diffraction-limited spot. Instead, we propose to use the derived analytic form for the image shape in eq 5 as a super-resolution fit function. Assuming that the observed dipole orientation is fixed relative to $\mathbf{d}$ by a polarizing filter,[23] eq 5 can be applied directly to experimental data using only $\mathbf{d}$ as a fit parameter. For an arbitrarily oriented molecular emitter, the fields presented in the Methods section for the three orthogonal dipole orientations can be weighted and summed to yield a more general analytic expression for the image where both d and the two angles specifying the molecular transition dipole orientation are fit parameters. As a proof of concept in the former case, the image shape on the right-hand side of eq 5 is fit to the diffraction-limited image produced by a full-wave numerical electrodynamics description of a dipole-driven gold nanosphere together with numerical evaluation of the Debye−Wolf diffraction integral. The performance of this new localization procedure is assessed by inference of the molecule position d by fitting both the analytic image function in eq 5 and a two-dimensional Gaussian function to the same electrodynamics simulation. These two procedures are contrasted in Figure 5 for two of the three unique dipole orientations; again the third orientation is identical to the $\perp$ case and is included in the SI. The average, maximum, and minimum mislocalization across $a + 5 \leq d \leq 350$ nm are presented for various spherical nanoantenna radii from 10−70 nm. Across all radii considered, the model fit is superior to the Gaussian fit, both in the average mislocalization and in the minimum and maximum localization errors.

In conclusion, we have presented a simple and intuitive theoretical model of plasmon-enhanced single-molecule fluorescence microscopy. The model draws on an analogy between Young's two-slit interference and a pair of radiating dipoles to organize the diffraction-limited image of the system into the superposition of three distinct contributions: the molecule PSF, nanoantenna PSF, and interference that can shift the intensity distribution toward or away from the center point between emitters. The relative weight of each resulting mislocalization is determined by the underlying microscopic coupled-dipole dynamics. Modeling the molecule−nanoantenna system by a pair of coupled oscillators accurately recovers the mislocalization calculated in full-wave electrodynamics simulation of a dipole-driven plasmonic nanoantenna. With this model, we draw on hybridization theory to discuss mislocalization from the perspective of mode mixing between molecule and plasmon degrees of freedom. We find that significant plasmon character is inherited by the hybrid modes at larger than expected separation distances due to the nanoantenna's significantly larger polarizability. Inspired by the Fano interference problem, we further derive an analytic measure of mislocalization that depends explicitly upon fundamental system parameters such as the relative separation, orientation, detuning, and polarizability of the emitters. This measure can be used to predict mislocalization without simulation, requiring only knowledge of the uncoupled emitters' emission/scattering spectra. Lastly, we propose a new model-based form of the plasmon-enhanced single-molecule fluorescence image that is appropriate for specified molecular dipole orientations and demonstrate that it significantly outperforms standard Gaussian fitting in locating the molecule's position in electrodynamics simulation. This

DOI: 10.1021/acsphotonics.8b00372
ACS Photonics XXXX, XXX, XXX−XXX

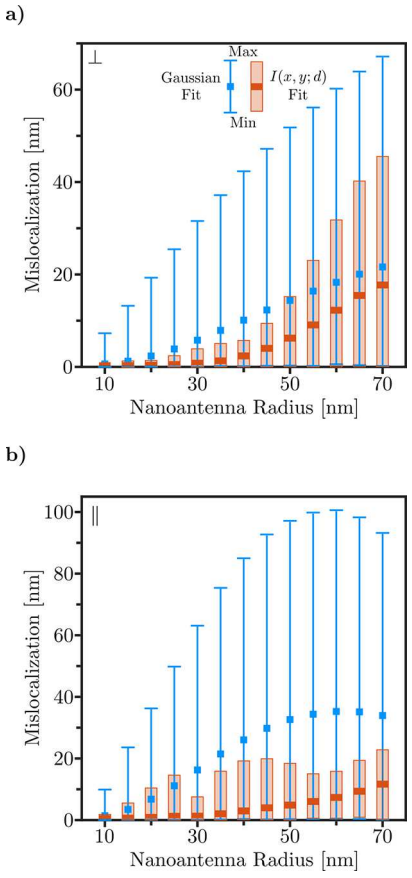

Figure 5. Extraction of molecule location from simulated plasmon-enhanced single-molecule fluorescence images using the analytic image function $I(x, y; d)$ (orange) derived in eq 5 and a two-dimensional Gaussian fit (blue). Both fitting methods are tested against molecule–nanoantenna separations $a + 5 \leq d \leq 350$ nm for a range of spherical nanoantenna radii a in both ∥ (a) and ⊥ (b) dipole orientations. For each radius, the average, minimum, and maximum mislocalization are determined by comparing d to the fit position d_0 in $I(x, y; d_0)$ or to the centroid position (x_0) in a two-dimensional Gaussian function. The corresponding average mislocalization is denoted as a rectangle and the minimum and maximum mislocalization are indicated by vertical bars. $I(x, y; d)$ in eq 5 and the two-dimensional Gaussian are both fit to the same set of numerical electrodynamics simulations of a dipole-driven gold nanoantenna in a vacuum. Across the wide range of nanoantenna radii sampled, fits to eq 5 provide a better estimate of molecule position than standard Gaussian fitting techniques.

model provides a clear path toward generalizing the fit function to account for unknown molecular orientation, which will form the basis for future work.

METHODS

Calculation and Analytic Approximation of Image Fields. The Debye–Wolf integral[40] allows accurate calculation of the PSF produced by diffraction-limited optical systems with large numerical aperture common in single-molecule fluorescence imaging.[41] For an idealized infinity-corrected microscope, the field composing the image is constructed by refraction at the objective lens and then focusing at a top lens into image space, where it is subject to diffraction. As outlined in ref 42, both the objective and top lens are considered spherical refracting surfaces with focal lengths f_{obj} and f, respectively. The objective is defined by spherical coordinates $(\xi_{obj}, \zeta_{obj}, f_{obj})$ relative to the antenna location. The top lens is defined by (ξ, ζ, f) relative to the focal point in image space.

The image field is related to the scattered field at the objective by

$$\mathbf{E}(\rho, \varphi, z) = -\frac{ikf\, e^{ikf}}{2\pi} \int_0^{\xi_m} d\xi \sin\xi \int_0^{2\pi} d\zeta \sqrt{\frac{\cos\xi}{\cos\xi_{obj}}} \times \mathbf{E}^{scat}(\xi, \zeta) e^{ik[\rho \sin\xi \cos(\varphi-\zeta)+(z-h)\cos\xi]} \tag{11}$$

The scattered field is evaluated at points on the objective by the relationship $\sin\xi = (f_{obj}/f)\sin\xi_{obj}$ and $\zeta = \zeta_{obj}$. The ratio of cosines appearing in the square root accounts for the two refractions. The term $e^{ik(z-h)\cos\xi}$ describes defocusing and defines the focal plane at $z = h$. The rotational symmetry of the lens/aperture allows analytic solution of the azimuthal ζ integral, leaving cylindrical Bessel functions. The remaining polar integral is evaluated numerically to produce images from all field data computed via full-wave electrodynamics simulation.

To obtain a simple closed form for the image fields, the numerical aperture is fixed at NA = 1 as well as the magnification, $f/f_{obj} = 1$. The effect of magnification can be restored theoretically by choosing a small, high-resolution image detection plane.[26] Under these conditions, the image field in the focal plane produced by a single dipole source located along the optical axis $(\hat{\mathbf{e}}_z)$ and oriented in (x, y)-plane is

$$\mathbf{E}_i(\rho, \varphi, z = h) = -ik^3 e^{2ikf} p_i \times \begin{pmatrix} [\cos^2(\varphi+\psi) + \cos(2\varphi+2\psi)]\frac{j_1(k\rho)}{k\rho} + \sin(\varphi+\psi)^2 j_0(k\rho) \\ \sin(\varphi+\psi)\cos(\varphi+\psi) j_2(k\rho) \\ -\cos(\varphi+\psi)\frac{J_2(k\rho)}{k\rho} \end{pmatrix} \tag{12}$$

where the dipole moment points at an angle ψ relative to $\hat{\mathbf{e}}_x$. For a dipole moment parallel to the optical axis, the field takes the form

$$\mathbf{E}_i(\rho, \varphi, z = h) = -ik^3 e^{2ikf} p_i \begin{pmatrix} -\cos(\varphi)\frac{J_2(k\rho)}{k\rho} \\ -\sin(\varphi)\frac{J_2(k\rho)}{k\rho} \\ \frac{2}{3}j_0(k\rho) - \frac{1}{3}j_2(k\rho) \end{pmatrix} \tag{13}$$

The analytic expressions for plasmon-enhanced single-molecule fluorescence images are obtained by summing the dipole image fields above with the molecule translated to match its location in the scattering plane, i.e.,

$$I(x, y; d) = \frac{c}{8\pi}|\mathbf{E}_0(x - d, y, z = h) + \mathbf{E}_1(x, y, z = h)|^2 \tag{14}$$

We have found that these analytic images are numerically equivalent to direct computation of the Debye–Wolf integral for the combined scattered field from both emitters. The analytic PSFs and interference function are obtained simply from the expansion of eq 14. The one-dimensional PSFs used throughout this paper are

DOI: 10.1021/acsphotonics.8b00372
ACS Photonics XXXX, XXX, XXX–XXX

$$f_{\mathrm{PSF}}^{\parallel}(x_i) = 4\left(\frac{j_1(kx_i)}{kx_i}\right)^2 + \left(\frac{J_2(kx_i)}{kx_i}\right)^2$$

$$f_{\mathrm{PSF}}^{\perp}(x_i) = \left(\frac{j_1(kx_i)}{kx_i} - j_0(kx_i)\right)^2 \tag{15}$$

and for the coaxial orientation,

$$f_{\mathrm{PSF}}^{\odot}(x_i) = \left(\frac{J_2(kx)}{kx}\right)^2 + \left(\frac{2}{3}j_0(kx_i) - \frac{1}{3}j_2(kx_i)\right)^2 \tag{16}$$

The one-dimensional interference function follows by replacing $x_i \to x - d$ and $x_i \to x$ in the first and second term, respectively, of each square as well as multiplication by 1/2.

Analytic Analysis of the Gaussian Mislocalization. To derive the parameters in eq 10, we start with the intensity evaluated along $(x, 0, h)$,

$$I(x; d) = \frac{ck^6}{8\pi}|p_0|^2\left(f_{\mathrm{PSF}}(x) + \left|\frac{p_1}{p_0}\right|^2 f_{\mathrm{PSF}}(x; d) + 2\mathrm{Re}\left[\frac{p_1}{p_0}\right] f_{\mathrm{IF}}(x; d)\right) \tag{17}$$

Note that, contrary to the main text, we have placed the molecule at the origin $x = 0$. It is then straightforward to split $I(x; d)$ into even and odd contributions about the molecule's position. Factoring out the even terms and noting that all resulting singularities are far outside the separation distances of interest, we have

$$I(x; d) = I_{\mathrm{even}}(x; d)\left[1 + \frac{I_{\mathrm{odd}}(x; d)}{I_{\mathrm{even}}(x; d)}\right] \tag{18}$$

We then Taylor expand both $I_{\mathrm{even}}(x, d)$ and $I_{\mathrm{odd}}(x, d)/I_{\mathrm{even}}(x; d)$ in powers of kx and approximate their functional forms by a Gaussian and a line, respectively. That is

$$I_{\mathrm{even}}(x; d) = I^{(0)} + \tfrac{1}{2}I^{(2)}(kx)^2 + \ldots \approx Ae^{-x^2/2\sigma^2}$$
$$\frac{I_{\mathrm{odd}}(x; d)}{I_{\mathrm{even}}(x; d)} = \eta kx + \ldots \tag{19}$$

Computing η is straightforward, as it is nothing more than a first-order expansion coefficient. To compute A and σ, we match expansion coefficients of $I_{\mathrm{even}}(x; d)$ with those of a Gaussian up to second order. Doing so, we find $A = I^{(0)}$ and $\sigma = (1/k)\sqrt{-I^{(0)}/I^{(2)}}$. All expansion coefficients are reported in the SI.

■ ASSOCIATED CONTENT

Supporting Information

The Supporting Information is available free of charge on the ACS Publications website at DOI: 10.1021/acsphotonics.8b00372.

Explicit functional dependence of the mislocalization measure's (eq 10) asymmetry parameter η and width σ upon basic system parameters; Figures S1 and S2 supporting Figures 3 and 5 in the main text (PDF)

■ AUTHOR INFORMATION

Corresponding Author

*E-mail: masiello@chem.washington.edu.

ORCID

Harrison J. Goldwyn: 0000-0002-7184-2120
Kevin C. Smith: 0000-0002-2397-1518
Jacob A. Busche: 0000-0003-4797-9415
David J. Masiello: 0000-0002-1187-0920

Author Contributions

D.J.M. conceived of and supervised the project. H.J.G., K.C.S., and D.J.M. designed the research. H.J.G., K.C.S., J.A.B., and D.J.M. wrote the manuscript.

Notes

The authors declare no competing financial interest.

■ ACKNOWLEDGMENTS

This work was supported by the University of Washington and the U.S. National Science Foundation under grant numbers NSF CHE-1727092 and CHE-1664684 (D.J.M.). This work was facilitated though the use of advanced computational, storage, and networking infrastructure provided by the Hyak supercomputer system at the University of Washington. The authors thank Prof. Katherine A. Willets and Prof. Joshua C. Vaughan for critical feedback on an early version of our manuscript.

■ REFERENCES

(1) Hell, S. W.; Wichmann, J. Breaking the Diffraction Resolution Limit by Stimulated Emission: Stimulated-emission-depletion Fluorescence Microscopy. *Opt. Lett.* **1994**, *19*, 780−782.

(2) Moerner, W.; Fromm, D. P. Methods of Single-Molecule Fluorescence Spectroscopy and Microscopy. *Rev. Sci. Instrum.* **2003**, *74*, 3597−3619.

(3) Rust, M. J.; Bates, M.; Zhuang, X. Sub-Diffraction-Limit Imaging by Stochastic Optical Reconstruction Microscopy (STORM). *Nat. Methods* **2006**, *3*, 793.

(4) Betzig, E.; Patterson, G. H.; Sougrat, R.; Lindwasser, O. W.; Olenych, S.; Bonifacino, J. S.; Davidson, M. W.; Lippincott-Schwartz, J.; Hess, H. F. Imaging Intracellular Fluorescent Proteins at Nanometer Resolution. *Science* **2006**, *313*, 1642−1645.

(5) Patterson, G.; Davidson, M.; Manley, S.; Lippincott-Schwartz, J. Superresolution Imaging Using Single-Molecule Localization. *Annu. Rev. Phys. Chem.* **2010**, *61*, 345−367.

(6) Deschout, H.; Zanacchi, F. C.; Mlodzianoski, M.; Diaspro, A.; Bewersdorf, J.; Hess, S. T.; Braeckmans, K. Precisely and Accurately Localizing Single Emitters in Fluorescence Microscopy. *Nat. Methods* **2014**, *11*, 253.

(7) Biteen, J.; Willets, K. A. Introduction: Super-Resolution and Single-Molecule Imaging. *Chem. Rev.* **2017**, *117*, 7241−7243.

(8) Huang, J.; Gumpper, K.; Chi, Y.; Sun, M.; Ma, J. Fast two-dimensional super-resolution image reconstruction algorithm for ultra-high emitter density. *Opt. Lett.* **2015**, *40*, 2989−2992.

(9) Fernández-Suárez, M.; Ting, A. Y. Fluorescent Probes for Super-Resolution Imaging in Living Cells. *Nat. Rev. Mol. Cell Biol.* **2008**, *9*, 929.

(10) Huang, B.; Bates, M.; Zhuang, X. Super-resolution fluorescence microscopy. *Annu. Rev. Biochem.* **2009**, *78*, 993−1016.

(11) Liu, Z.; Lavis, L. D.; Betzig, E. Imaging Live-Cell Dynamics and Structure at the Single-Molecule Level. *Mol. Cell* **2015**, *58*, 644−659.

(12) Chozinski, T. J.; Gagnon, L. A.; Vaughan, J. C. Twinkle, Twinkle Little Star: Photoswitchable Fluorophores for Super-Resolution Imaging. *FEBS Lett.* **2014**, *588*, 3603−3612.

(13) Minoshima, M.; Kikuchi, K. Photostable and Photoswitching Fluorescent Dyes for Super-Resolution Imaging. *JBIC, J. Biol. Inorg. Chem.* **2017**, *22*, 639−652.

(14) Kinkhabwala, A.; Yu, Z.; Fan, S.; Avlasevich, Y.; Müllen, K.; Moerner, W. Large Single-Molecule Fluorescence Enhancements Produced by a Bowtie Nanoantenna. *Nat. Photonics* **2009**, *3*, 654.

DOI: 10.1021/acsphotonics.8b00372
ACS Photonics XXXX, XXX, XXX−XXX

(15) Flynn, J. D.; Haas, B. L.; Biteen, J. S. Plasmon-Enhanced Fluorescence from Single Proteins in Living Bacteria. *J. Phys. Chem. C* **2016**, *120*, 20512−20517.
(16) Lee, S. A.; Biteen, J. S. Interplay of Nanoparticle Resonance Frequency and Array Surface Coverage in Live-Cell Plasmon-Enhanced Single-Molecule Imaging. *J. Phys. Chem. C* **2018**, *122*, 5705−5709.
(17) Willets, K. A.; Wilson, A. J.; Sundaresan, V.; Joshi, P. B. Super-Resolution Imaging And Plasmonics. *Chem. Rev.* **2017**, *117*, 7538−7582.
(18) Wertz, E.; Isaacoff, B. P.; Flynn, J. D.; Biteen, J. S. Single-Molecule Super-Resolution Microscopy Reveals How Light Couples to a Plasmonic Nanoantenna on the Nanometer Scale. *Nano Lett.* **2015**, *15*, 2662−70.
(19) Blythe, K. L.; Willets, K. A. Super-Resolution Imaging of Fluorophore-Labeled DNA Bound to Gold Nanoparticles: A Single-Molecule, Single-Particle Approach. *J. Phys. Chem. C* **2016**, *120*, 803−815.
(20) Raab, M.; Vietz, C.; Stefani, F. D.; Acuna, G. P.; Tinnefeld, P. Shifting Molecular Localization by Plasmonic Coupling in a Single-molecule Mirage. *Nat. Commun.* **2017**, *8*, 13966.
(21) Fu, B.; Isaacoff, B. P.; Biteen, J. S. Super-Resolving the Actual Position of Single Fluorescent Molecules Coupled to a Plasmonic Nanoantenna. *ACS Nano* **2017**, *11*, 8978−8987.
(22) Wertz, E. A.; Isaacoff, B. P.; Biteen, J. S. Wavelength-Dependent Super-resolution Images of Dye Molecules Coupled to Plasmonic Nanotriangles. *ACS Photonics* **2016**, *3*, 1733−1740.
(23) Ropp, C.; Cummins, Z.; Nah, S.; Fourkas, J. T.; Shapiro, B.; Waks, E. Nanoscale Probing of Image-Dipole Interactions in a Metallic Nanostructure. *Nat. Commun.* **2015**, *6*, 6558.
(24) Lim, K.; Ropp, C.; Barik, S.; Fourkas, J.; Shapiro, B.; Waks, E. Nanostructure-Induced Distortion in Single-Emitter Microscopy. *Nano Lett.* **2016**, *16*, 5415−5419.
(25) Su, L.; Yuan, H.; Lu, G.; Rocha, S.; Orrit, M.; Hofkens, J.; Uji-i, H. Super-Resolution Localization and Defocused Fluorescence Microscopy on Resonantly Coupled Single-Molecule, Single-Nanorod Hybrids. *ACS Nano* **2016**, *10*, 2455−2466.
(26) Heaps, C. W.; Schatz, G. C. Modeling Super-Resolution SERS Using a T-matrix Method to Elucidate Molecule-Nanoparticle Coupling and The Origins of Localization Errors. *J. Chem. Phys.* **2017**, *146*, 224201.
(27) Fano, U. Effects of configuration interaction on intensities and phase shifts. *Phys. Rev.* **1961**, *124*, 1866.
(28) Cherqui, C.; Bigelow, N. W.; Vaschillo, A.; Goldwyn, H.; Masiello, D. J. Combined Tight-Binding and Numerical Electrodynamics Understanding of the STEM/EELS Magneto-optical Responses of Aromatic Plasmon-Supporting Metal Oligomers. *ACS Photonics* **2014**, *1*, 1013−1024.
(29) Cherqui, C.; Thakkar, N.; Li, G.; Camden, J. P.; Masiello, D. J. Characterizing Localized Surface Plasmons Using Electron Energy-Loss Spectroscopy. *Annu. Rev. Phys. Chem.* **2016**, *67*, 331−57.
(30) Anger, P.; Bharadwaj, P.; Novotny, L. Enhancement and Quenching of Single-Molecule Fluorescence. *Phys. Rev. Lett.* **2006**, *96*, 113002.
(31) Nie, S.; Emory, S. Probing Single Molecules and Single Nanoparticles by Surface-Enhanced Raman Scattering. *Science* **1997**, *275*, 1102.
(32) Kneipp, K.; Wang, Y.; Kneipp, H.; Perelman, L. T.; Itzkan, I.; Dasari, R. R.; Feld, M. S. Single Molecule Detection Using Surface-Enhanced Raman Scattering (SERS). *Phys. Rev. Lett.* **1997**, *78*, 1667.
(33) Masiello, D. J.; Schatz, G. C. Many-body theory of surface-enhanced Raman scattering. *Phys. Rev. A: At., Mol., Opt. Phys.* **2008**, *78*, 042505.
(34) Camden, J. P.; Dieringer, J. A.; Wang, Y.; Masiello, D. J.; Marks, L. D.; Schatz, G. C.; Van Duyne, R. P. Probing the Structure of Single-Molecule Surface-Enhanced Raman Scattering Hot Spots. *J. Am. Chem. Soc.* **2008**, *130*, 12616.
(35) Novotny, L., Hecht, B., Eds. *Principles of Nano-Optics*; Cambridge University Press: Cambridge, 2006.
(36) Link, S.; El-Sayed, M. A. Spectral Properties and Relaxation Dynamics of Surface Plasmon Electronic Oscillations in Gold and Silver Nanodots and Nanorods. *J. Phys. Chem. B* **1999**, *103*, 8410−8426.
(37) Mack, D. L.; Cortés, E.; Giannini, V.; Török, P.; Roschuk, T.; Maier, S. A. Decoupling Absorption and Emission Processes in Super-Resolution Localization of Emitters in a Plasmonic Hotspot. *Nat. Commun.* **2017**, *8*, 14513.
(38) Thakkar, N.; Rea, M. T.; Smith, K. C.; Heylman, K. D.; Quillin, S. C.; Knapper, K. A.; Horak, E. H.; Masiello, D. J.; Goldsmith, R. H. Sculpting Fano Resonances To Control Photonic-Plasmonic Hybridization. *Nano Lett.* **2017**, *17*, 6927−6934.
(39) Baldwin, C. L.; Bigelow, N. W.; Masiello, D. J. Thermal Signatures of Plasmonic Fano Interferences: Toward the Achievement of Nanolocalized Temperature Manipulation. *J. Phys. Chem. Lett.* **2014**, *5*, 1347−1354.
(40) Wolf, E. Electromagnetic Diffraction in Optical Systems-I. An Integral Representation of the Image Field. *Proc. R. Soc. London, Ser. A* **1959**, *253*, 349−357.
(41) Dhayalan, V.; Stamnes, J. J. Focusing of Electric-Dipole Waves in the Debye And Kirchhoff Approximations. *Pure Appl. Opt.* **1997**, *6*, 347.
(42) Hoang, T. X.; Duan, Y.; Chen, X.; Barbastathis, G. Focusing and Imaging In Microsphere-Based Microscopy. *Opt. Express* **2015**, *23*, 12337−53.

DOI: 10.1021/acsphotonics.8b00372
ACS Photonics XXXX, XXX, XXX−XXX